



Potential effect of the marine carbon cycle on the multiple equilibria window of the Atlantic Meridional Overturning Circulation

Amber A. Boot¹, Anna S. von der Heydt^{1,2}, and Henk A. Dijkstra^{1,2}

¹Institute for Marine and Atmospheric research Utrecht, Department of Physics, Utrecht University, Utrecht, the Netherlands

²Center for Complex Systems Studies, Utrecht University, Utrecht, the Netherlands

Correspondence: Amber A. Boot (a.a.boot@uu.nl)

Abstract. The Atlantic Meridional Overturning Circulation (AMOC) is considered to be a tipping element in the Earth System due to possible multiple (stable) equilibria. Here, we investigate the multiple equilibria window of the AMOC within a coupled ocean circulation-carbon cycle box model. We show that adding couplings between the ocean circulation and the carbon cycle model affects the multiple equilibria window of the AMOC. Increasing the total carbon content of the system widens the multiple equilibria window of the AMOC, since higher atmospheric pCO₂ values are accompanied by stronger freshwater forcing over the Atlantic Ocean. The important mechanisms behind the increase of the multiple equilibria window are the balance between the riverine source and the sediment sink of carbon and the sensitivity of the AMOC to freshwater forcing over the Atlantic Ocean. Our results suggest that changes in the marine carbon cycle can influence AMOC stability in future climates.

10 1 Introduction

The Atlantic Meridional Overturning Circulation (AMOC) plays a large role in modulating global climate (Vellinga and Wood, 2008; Palter, 2015) because it transports heat from the Southern to the Northern Hemisphere and is one of the prominent tipping elements in the Earth System (Lenton et al., 2008; Armstrong-McKay et al., 2022). Model studies suggest that the AMOC can have multiple stable equilibria: the on-state, representing the current AMOC state with a strong northward flow at the surface and a southward return flow at intermediate depths; and the off-state, representing a weak or even reversed AMOC state (Weijer et al., 2019). From a dynamical systems point of view, a bi-stable AMOC regime appears through the occurrence of two saddle node bifurcations (Dijkstra, 2007) and the region in parameter space where both on- and off-states co-exist is the multiple equilibria window (MEW), also referred to as the bi-stability window (Barker and Knorr, 2021).

Climate variability in the past, such as Heinrich events, has been linked to tipping of the AMOC (Rahmstorf, 2002; Lynch-Stieglitz, 2017). Under anthropogenic forcing, the global warming threshold for AMOC tipping has been recently estimated to be around 4 °C (Armstrong-McKay et al., 2022). Using model data from the Coupled Model Intercomparison Project 6 (CMIP6, Eyring et al., 2016), a consistent weakening of the AMOC under future climate change is projected (Weijer et al., 2020), with a 34-45% decrease in AMOC strength in 2100, but no clear tipping was found. However, these models may have a too stable AMOC (Weijer et al., 2019) affecting the probability of AMOC tipping before 2100. Under AMOC tipping, a strong



25 cooling in the Northern Hemisphere (Rahmstorf, 2002; Drijfhout, 2015), changes in the water cycle (Vellinga and Wood, 2002; Jackson et al., 2015), and potential interactions with other tipping elements in the Earth System (Dekker et al., 2018; Wunderling et al., 2021; Sinet et al., 2023) are expected.

The AMOC can also interact with the marine carbon cycle and therefore influence atmospheric $p\text{CO}_2$. By affecting the transport of important tracers, such as dissolved inorganic carbon (DIC), total alkalinity, and nutrients, the AMOC affects the solubility and biological carbon pumps. Evidence for a coupling between the AMOC and marine carbon cycle is provided in proxy data (Bauska et al., 2021). Model studies show a wide range of potential carbon cycle responses to a collapse of the AMOC. While most models show an increase in atmospheric $p\text{CO}_2$ (e.g., Marchal et al., 1998; Schmittner and Galbraith, 2008; Matsumoto and Yokoyama, 2013), the magnitude and precise mechanisms are dependent on the model used and climatic boundary conditions (Gottschalk et al., 2019).

35 As the AMOC can influence atmospheric $p\text{CO}_2$, there is a potential feedback mechanism since atmospheric $p\text{CO}_2$ influences the hydrological cycle (Weijer et al., 2019; Barker and Knorr, 2021), which through changes in buoyancy fluxes, affects the AMOC. Previous studies suggest that there may be a relation between atmospheric $p\text{CO}_2$ and the MEW of the AMOC (Barker et al., 2010, 2015). However, a clear mechanistic view has not been given yet. Here, we study the mechanisms on how the marine carbon cycle can affect the MEW of the AMOC using a coupled ocean circulation-carbon cycle box model.

40 2 Methods

We have coupled a box model suitable for simulating AMOC dynamics (Section 2.1) to a carbon cycle box model (Section 2.2). To be able to accurately represent atmospheric CO_2 concentrations, the coupled model extends the AMOC box model by including boxes that represent the Indo-Pacific. Steady states of the coupled model, where several non-linear couplings are implemented (Section 2.3), are determined using continuation software (Section 2.4). Parameter values and model equations are described in Appendices B and C.

2.1 AMOC box model

The box model (Cimatoribus et al., 2014; Castellana et al., 2019) representing the AMOC dynamics simulates the depth of the Atlantic Ocean pycnocline, and the distribution of salt in the Atlantic Ocean and the Southern Ocean. It consists of 5 boxes, with 6 prognostic variables. The northern box n represents the regions of deep water formation in the North Atlantic and box s represents the entire Southern Ocean (i.e. all longitudes). There are two thermocline boxes t and ts where box ts represents the region between 30°S and 40°S which is characterized by strong sloping isopycnals where the pycnocline becomes shallower moving poleward. Underneath the four surface boxes, there is one box (d) representing the deep ocean.

The distribution of salinity in the boxes is dependent on the ocean circulation and surface freshwater fluxes. In the Southern Ocean, there is wind-induced Ekman transport into the Atlantic (q_{Ek}), and there is an eddy induced transport from the Atlantic into the Southern Ocean (q_e) which is dependent on the pycnocline depth D . The difference between the two, defined as $q_S = q_e - q_{Ek}$, represents upwelling in the Southern Ocean and net volume transport into the Atlantic thermocline. The thermocline



also is sourced with water from box d through diffusive upwelling (q_U). The strength of the downward branch of the AMOC is represented in the North Atlantic by q_N . This downwelling is dependent on the meridional density gradient between box ts and box n , where the density is determined using a linear equation of state. Wind driven gyre transport is modelled by r_N in the Northern Hemisphere, and r_S in the Southern Hemisphere. Salinity is also affected by two surface freshwater fluxes, modelled as virtual salt fluxes. First, there is a symmetrical forcing E_s , i.e. this freshwater flux is the same for both hemispheres; and secondly, there is an asymmetrical forcing E_a which results in interhemispheric differences. This last parameter can be viewed as a control parameter for the AMOC strength since it regulates the salinity of box n . The pycnocline depth is an important state variable in this model since several volume fluxes are dependent on it. This depth is dependent on four different volume fluxes going in and out of the two thermocline boxes t and ts (q_e, q_{Ek}, q_U, q_N).

The model provides a simple framework to study AMOC dynamics and has already been used to show both slow (Cimatoribus et al., 2014) and fast, noise-induced (Castellana et al., 2019; Jacques-Dumas et al., 2023) tipping of the AMOC.

2.2 Carbon cycle model

The carbon cycle model is derived from the equations of the SCP-M (O'Neill et al., 2019). The original SCP-M has two terrestrial carbon stocks, an atmosphere box, and 7 ocean boxes representing the global ocean. In the ocean multiple tracers are simulated that are important for the marine carbon cycle. In this study, we only simulate dissolved inorganic carbon (DIC), alkalinity (Alk) and phosphate (PO_4) in the ocean. All three tracers are affected by ocean circulation, have a riverine source and a sink to the sediments. DIC is affected by biological production and remineralization (soft tissue pump), the formation and dissolution of calcium carbonate ($CaCO_3$; carbonate pump), and gas exchange with the atmosphere. Alk is also affected by the carbonate pump, and PO_4 by the soft tissue pump. In this model, PO_4 is explicitly conserved, i.e. the source of PO_4 is equal to the sink of PO_4 at all times. DIC and Alk, however, can vary since the time dependent riverine influx is not necessarily equal to the sediment outflux.

The soft tissue pump is modelled using constant values of export production per box, and the remineralization in the water column follows a power law (Martin et al., 1987). The influence of the soft tissue pump on the cycling of PO_4 is modelled using a constant stoichiometric ratio. The formation of $CaCO_3$ is proportional to the export production times a constant rain ratio parameter. $CaCO_3$ is dissolved through the water column and in the sediments. This dissolution is dependent on the $CaCO_3$ saturation state, and a constant background dissolution. The gas exchange between the ocean and atmosphere is dependent on a constant piston velocity and the difference in pCO_2 between the two reservoirs. The riverine influx of PO_4 is constant, whereas the influx of DIC and Alk is dependent on atmospheric pCO_2 .

2.3 Coupled model

The two models described in the previous section are coupled forming the model used in this study (Fig. 1). For this, several parameter assumptions had to be made, since the carbon cycle model requires more parameters than the AMOC model. First of all, the depth of boxes n and s is not given in Cimatoribus et al. (2014) but is necessary for the carbon cycle model. We



90 assume these to be 300 m, and the total depth of the ocean is assumed to be 4000 m. Secondly, a first version of the model showed a too strong sensitivity of atmospheric CO₂ concentrations to AMOC tipping causing very low CO₂ concentrations on the AMOC off-branch. We therefore have included two additional boxes in the AMOC model representing the Indo-Pacific basin: box *ps* for the surface ocean and box *pd* for the deep ocean. In these boxes the same carbon cycle processes are present as in the Atlantic and Southern Ocean boxes of the model. Between these two boxes there is a bidirectional mixing term ($\gamma_1 =$
 95 30 Sv), and the boxes are connected with the Southern Ocean through a Global Overturning Circulation (GOC; $\psi_1 = 18$ Sv), and gyre-driven exchange ($r_P = 90$ Sv). γ_1 and ψ_1 are taken from the SCP-M (O'Neill et al., 2019), and r_P is based on the model of Wood et al. (2019). Both box *t* and *ps* receive DIC, Alk and PO₄ input through a river flux. The total river flux is modelled similarly as in the SCP-M and is partitioned over the two boxes based on the volume fraction of the Atlantic Ocean and the Indo-Pacific Ocean, meaning 20% of the river flux flows into box *t*, while the remainder flows into box *ps*.

100 The first coupling between the physical and the carbon cycle model is through the ocean circulation. The AMOC determined in the circulation model is used for the advective transport of the three tracers in the carbon cycle model. We have implemented additional couplings between the model and specific feedbacks within the carbon cycle model. Several of these feedbacks have been introduced into the SCP-M before (Boot et al., 2022).

105 Firstly, we create a dependency of the biological export production in the surface boxes to the amount of PO₄ advected into the specific surface box and therefore introducing a dependency on the ocean circulation

$$Z_i = (1 - \lambda_{BI}) \times Z_{i,base} + \lambda_{BI} \times (q_{j \rightarrow i} \times [PO_4^{3-}]_j + P_{river}) \times \epsilon_i. \quad (1)$$

Here Z_i represents the export production in surface box *i*, λ_{BI} a parameter to switch between the default value of Z in box *i* ($Z_{i,base}$; $\lambda_{BI} = 0$) and the variable export production ($\lambda_{BI} = 1$). In addition, $q_{j \rightarrow i}$ represents the volume transport from box *j* into box *i*. P_{river} the riverine influx of PO₄, which is only present in boxes *t* and *ps*, and ϵ_i represents a biological efficiency
 110 term in box *i*. *i* represents all surface boxes, i.e. *n*, *t*, *ts*, *s* and *ps*. *j* can be any box and depends on the direction of the ocean circulation.

We also introduce a coupling between the symmetric freshwater forcing E_s and atmospheric pCO₂. This coupling is based on a fit to an ensemble of CMIP6 Earth System Models and is described in Section 3.1.

115 We allow the sea surface temperatures (SSTs) to vary with atmospheric pCO₂ following a logarithmic function and a climate sensitivity parameter, according to

$$T_i = T_{i,base} + \Delta T_i, \quad (2)$$

$$\Delta T_i = \lambda_T \times 0.54 \times 5.35 \ln\left(\frac{CO_2}{CO_{2,0}}\right). \quad (3)$$

120 Here *i* represents the different surface ocean boxes. By varying the parameter λ_T we are able to change the climate sensitivity of the model. In this study we use a value of $\lambda_T = 0$ (default), $\lambda_T = 1$ (CS_{LO}) and a value of $\lambda_T = 2$ (CS_{HI}), representing SST

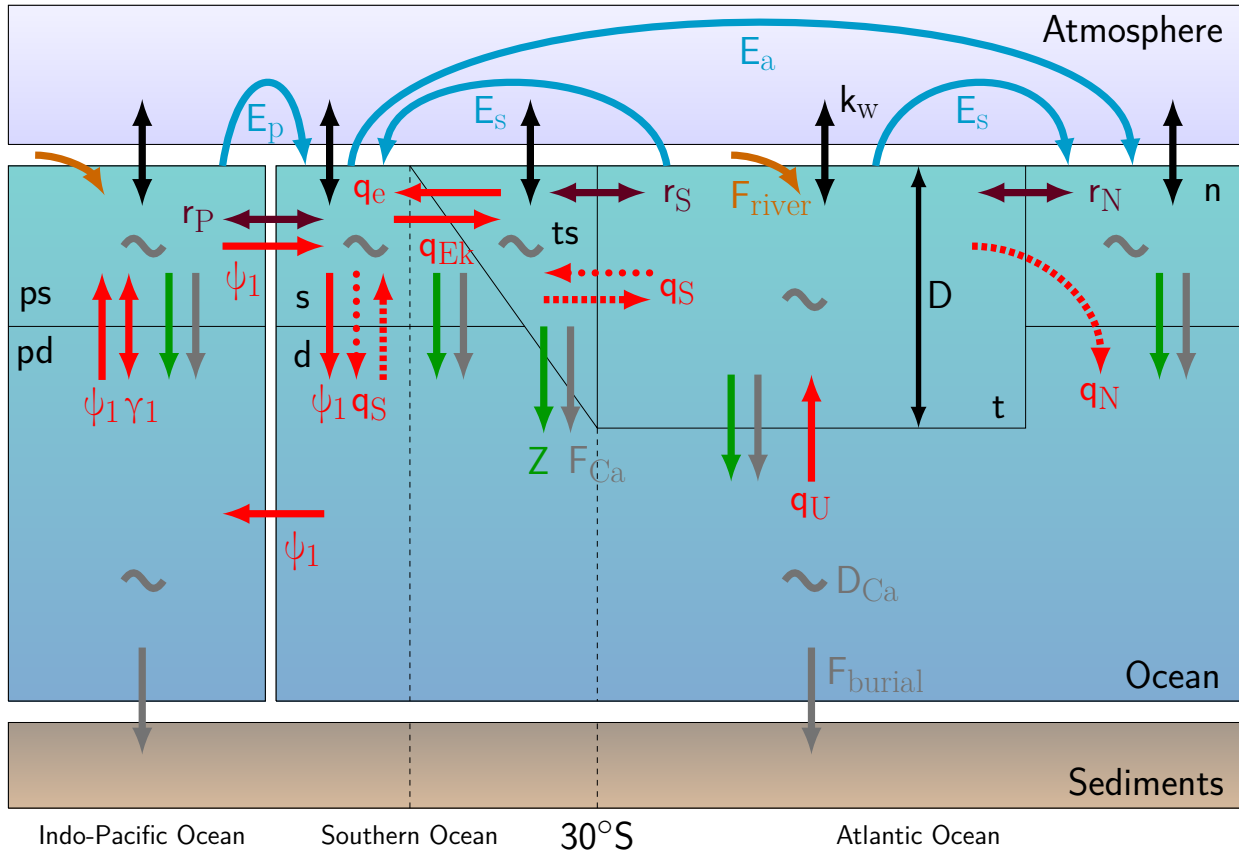


Figure 1. Box structure and processes simulated in the coupled circulation – carbon cycle model. Red arrows represent volume transports where dashed arrows are only present during an on-state, and dotted arrows only present during an off-state. The purple arrows represent gyre exchange (r_N , r_S , and r_P), and blue arrows freshwater fluxes (E_s , E_a , and E_p). Carbon cycle processes that are represented are riverine input (orange), air-sea gas exchange (black; k_w), biological export production (green; Z), CaCO_3 rain (grey; F_{Ca}), CaCO_3 dissolution (grey; D_{Ca}), and sediment burial (grey; F_{burial}). Based on Castellana et al. (2019) and Boot et al. (2022).

warming of 0 K, 2 K and 4 K per CO_2 doubling. For the default values, sea surface temperature remains constant independent of atmospheric pCO_2 values. For surface air temperature in CMIP6 models, the response to a CO_2 doubling is between 1.8 and 5.6 K (Zelinka et al., 2020). When this coupling is used, the changes in SSTs will also change the density in the ocean circulation model. However, since we use a linear equation of state and the change of SST is homogeneous over all surface boxes, it does not influence the ocean circulation.



Lastly, we have introduced a coupling on the rain ratio (Eq. 4) making it dependent on the saturation state of CaCO_3 following

$$F_{Ca,i} = (1 - \lambda_F) \times F_{Ca,base} + \lambda_F \times 0.022 \left(\frac{[Ca_i^{2+}][CO_3^{2-}]}{K_{sp,i}} \right)^{0.81}, \quad (4)$$

where i represents the different surface ocean boxes. Similar to the biological coupling coefficient λ_{BI} , λ_F is either 0 or 1, and including this feedback will introduce different rain ratios per box.

We have included additional couplings in the model that are described in Appendix A. They are not included in the main text since they do not show large effects on the results. In the main text only the couplings described above are used. We refer to the couplings as BIO for the biological coupling (BIO), E_s for the E_s -coupling described in Section 3.1, FCA for the rain ratio coupling, CS_{LO} for a low climate sensitivity and CS_{HI} for a high climate sensitivity.

2.4 Solution method

The coupled model is a system of 30 ODEs (four tracers per box, the pycnocline depth and atmospheric pCO_2) of the form

$$\frac{d\mathbf{u}}{dt} = f(\mathbf{u}(t), \mathbf{p}). \quad (5)$$

Here \mathbf{u} is the state vector (containing all the dependent quantities in all boxes), f contains the right-hand-side of the equations and \mathbf{p} is the parameter vector. To solve this system of equations we use the continuation software AUTO-07p (Doedel et al., 2007). Both the AMOC model (Cimatoribus et al., 2014), and the SCP-M (Boot et al., 2022) have already been implemented in this software. AUTO enables us to efficiently compute branches of stable and unstable steady state solutions under a varying control parameter. Furthermore, it allows for detection of special points such as saddle-node bifurcations, here important for determining the multiple equilibria window of the AMOC.

One of the requirements of AUTO is that the Jacobian of the system (5) is non-singular at non-bifurcation points. To achieve this, we use explicit conservation equations to eliminate the ODEs of the deep Atlantic box (d). Both the conservation equation of salt and PO_4 are already explicitly included into the model. However, as described previously, this is not the case for DIC and Alk. Therefore, we have to introduce extra ODEs describing the change in total carbon and alkalinity in the system. The change in total carbon (DIC + atmospheric CO_2) and Alk in the atmosphere-ocean system can be captured as the sum of riverine influx and the sediment outflux. The riverine influx is a function of atmospheric pCO_2 and represents the weathering of silicate and carbonate rocks i.e.,

$$C_{river} = W_{carb,c} + (W_{carb,v} + W_{si}) \times CO_2^{atm}. \quad (6)$$

The sediment outflux of DIC is determined by the sum of the soft tissue and the carbonate pumps over the entire ocean. In this model, all produced organic matter is also remineralized in the water column, causing the contribution of the soft tissue pump to be negligible resulting in



$$155 \quad C_{sed} = C_{river} \times V_t + \sum_{i=1}^7 (C_{carb,i} \times V_i). \quad (7)$$

Since the change in alkalinity in the system is proportional to the change in total carbon, only one extra ODE is necessary. By eliminating the ODEs for the deep box and introducing the ODE for total carbon in the ocean-atmosphere system, AUTO eventually solves a system with 27 ODEs.

The use of AUTO made it necessary to make changes in the carbonate chemistry of the carbon cycle model. In the original
160 SCP-M a simple time dependent function is used where the pH of timestep k-1 is used as an initial guess for timestep k (Follows et al., 2006). As long as the changes per time step remain relatively small, this scheme is sufficiently accurate. However, due to our solution method, in which steady states are calculated versus parameters, this function is not suitable for this study. Therefore, we have chosen a simple ‘text-book’ carbonate chemistry (Williams and Follows, 2011; Munhoven, 2013) where Alk is assumed to be equal to carbonate alkalinity ($Alk_{carb} = [HCO_3^-] + [CO_3^{2-}]$). This method is less accurate and leads to
165 higher pH values (Munhoven, 2013) and lower atmospheric pCO₂ values (Boot et al., 2022). To address the lower resulting atmospheric pCO₂ values we have increased the value of the constant rain ratio from 0.07 as used in the original SCP-M to 0.15.

AUTO has three parameters that determine the accuracy of the solution. The absolute and relative accuracy are set to a base value of 10⁻⁶, but sometimes a higher accuracy is used. The accuracy for the detection of special points (e.g. saddle-nodes and
170 Hopf bifurcations) is set to 10⁻⁷.

3 Results

3.1 CMIP6 freshwater fluxes

The freshwater fluxes E_s and E_p used in the model are constrained using results from a CMIP6 ensemble. For this we use 28
175 different CMIP6 models forced with a 1% increase per year in atmospheric CO₂ concentrations (‘1pctco2’). We integrate the variables ‘wfo’ (water flux) and ‘vsf’ (virtual salt flux) over the regions representing the Atlantic thermocline (Atlantic basin between 30°S and 50°N) and the Indo-Pacific basin (the rest of the ocean north of 30°S and south of 66°N) in the coupled box model. Based on these 28 models we determine a multimodel mean and we are able to constrain both E_p and E_s .

Fig. 2a shows that most models, and the multimodel mean, show no, or at most a very weak relation between E_p and atmospheric pCO₂, whereas there seems to be a relation between E_s and atmospheric pCO₂. For E_p we will use the mean
180 value over the entire simulation (0.99 Sv). For E_s we will use as a default value 0.39 Sv since this is the value of E_s at pCO_{2,0} (320 ppm). Furthermore, we introduce an additional coupling in the model where we implement E_s as a function of atmospheric pCO₂ based on a logarithmic fit to represent the relation between E_s and atmospheric pCO₂ present in the CMIP6 ensemble. This relation is modelled as:



$$E_s = (1 - \lambda_E) \times E_{s,base} + \lambda_E \times (-0.142 + 0.097 \times \ln(CO_2)) \quad (8)$$

185 Here λ_E is a parameter controlling whether the coupling is used ($\lambda_E = 1$) or the default value of $E_{s,base}$ (0.39 Sv) is used
($\lambda_E = 0$). Compared to earlier versions of the model we will use a different default value for E_s . In previous studies values
of 0.25 Sv (Cimatoribus et al., 2014) and 0.17 Sv (Castellana et al., 2019) have been used. Here we choose the default value
based on the value of E_s at an atmospheric pCO_2 value of 320 ppm ($pCO_{2,0}$) in the CMIP6 fit. The value of 0.39 Sv is of the
same order as seen in the HOPAS4.0 dataset based on satellite observations Andersson et al. (2017). This dataset shows a net
190 freshwater flux of 1 Sv averaged over the period 1987-2015 into the region representing the thermocline box, which results in
an E_s value of 0.5 Sv.

We have made two important choices for using these CMIP6 constrained freshwater fluxes. First of all, we set the freshwater
transport through the atmosphere from the Atlantic to the Indo-Pacific basin to 0. There are studies showing there is moisture
195 transport between the two basins through the atmosphere (e.g., Dey and Döös, 2020), but it is challenging to constrain this flux
from Earth System Models. However, in our model set up, the exact value of this flux is not relevant for our results. The total
freshwater flux integrated over the Indo-Pacific basin diagnosed from the CMIP6 ensemble is independent from the moisture
transport between the Atlantic and Indo-Pacific basin. By rescaling the freshwater flux from the Indo-Pacific basin (box ps)
to the Southern Ocean (box s) we can set the freshwater flux from the Atlantic to the Indo-Pacific to 0 without changing the
200 AMOC dynamics. Tests where this flux was not set to 0, but net evaporation out of boxes t and ps were kept constant show
this. The only effect of this freshwater transport is a shift of the diagram along the E_a axis and a small effect on atmospheric
 pCO_2 of a couple of ppm due to salinity changes.

The second choice we have made is that the net evaporation from the Atlantic thermocline is symmetrically divided over the
northern and southern high latitudes. For this model, the exact direction of the freshwater flux out of box t is irrelevant. What
205 is relevant is the total freshwater flux at each surface box. Through this we can see that the asymmetric freshwater flux, E_a ,
creates an asymmetry in freshwater forcing over the Atlantic basin. Through this, E_a creates the asymmetry that is potentially
more realistic. Since we use E_a as our control parameter in the continuations, we do not need to constrain this parameter.

3.2 The AMOC multiple equilibria window

In Fig. 3 the bifurcation diagrams for the AMOC strength (Fig. 3a, c) and atmospheric pCO_2 (Fig. 3b, d) versus E_a are shown
210 for 6 different model configurations. The model configurations are differentiated on feedbacks and couplings included (see
Table 1). The bifurcation diagrams show that to be able to simulate both the on- and off-branch, it is vital that the BIO coupling
is used. When this coupling is not used, PO_4 concentrations will become negative in the surface ocean under a collapsed
AMOC regime. This behavior is illustrated in Fig. 3a, b by the cases REF and BIO. In case REF the off-branch (with negative
 PO_4) is not shown, while for case BIO the full bifurcation diagram with two saddle-node bifurcations is plotted. In Fig. 3b,
215 d we can also see the effect of AMOC tipping on atmospheric pCO_2 . On both the on- and the off-branch, atmospheric pCO_2

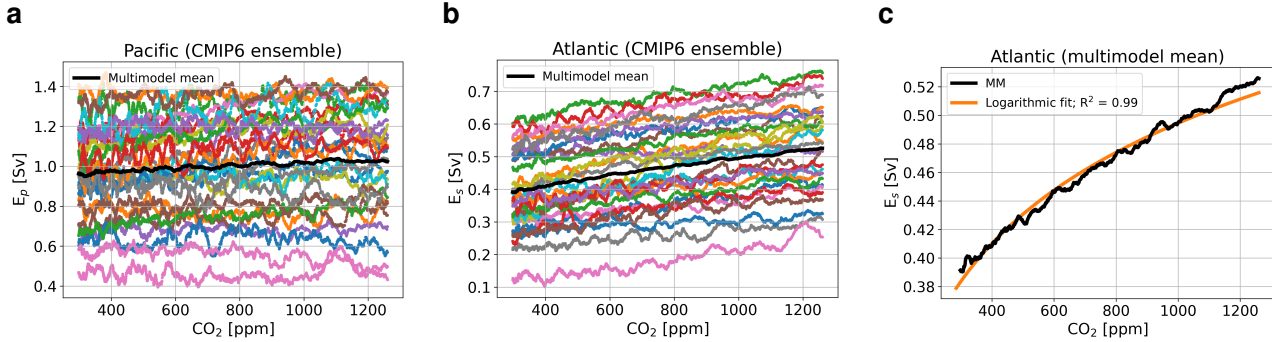


Figure 2. (a) Net evaporation from the Indo-Pacific basin representing the freshwater flux E_p in Sv for the CMIP6 ensemble with the multimodel mean in black. (b) As in (a) but for the freshwater flux E_s . (c) The multimodel mean for E_s in black with a logarithmic fit in orange.

Table 1. Overview of the used cases. The left column represents the name of the case. The other columns represent whether a coupling denoted in the top row is used in the case mentioned in the first column by indicating the λ parameter associated to the coupling. For λ_T the value represents the strength of the coupling.

Case name	λ_{BI}	λ_E	λ_F	λ_T
REF	0	0	0	0
BIO	1	0	0	0
E_s + BIO	1	1	0	0
E_s + BIO + FCA	1	1	1	0
E_s + BIO + FCA + CS_{LO}	1	1	1	1
E_s + BIO + FCA + CS_{HI}	1	1	1	2

values are relatively constant and the difference between the branches is approximately 25 to 40 ppm depending on the exact case, values that are of the same order as values reported in more complex models (Gottschalk et al., 2019).

To explain the lower pCO_2 values on the off-branch we consider the constraint in the model on total carbon content in the ocean-atmosphere system. In steady state, the riverine input and sediment outflux of DIC must balance to keep the total carbon content constant (in steady state). In our model, the sediment outflux is a function of the saturation state of $CaCO_3$ and $CaCO_3$ flux which is a function of the rain ratio (constant in non-FCA cases) and the export production. However, in the AMOC off state, the saturation state of $CaCO_3$ in the ocean is in every box larger than 1, meaning that there is no saturation driven dissolution of $CaCO_3$ and the sediment outflux is purely a function of the export production and a constant background dissolution rate. In an AMOC off-state, nutrient advection is relatively low causing a reduction in export production, and therefore a smaller sediment outflux. In steady state, the riverine influx must balance this small outflux, which is only possible by decreasing atmospheric pCO_2 values.



From the 6 cases considered here (Table 1) we can see the effect of the individual couplings. As described earlier, the biological coupling is necessary to determine the off-branch but does not influence the bifurcation diagrams otherwise. The rain ratio coupling (FCA) decreases atmospheric CO₂ concentrations by 35 ppm and slightly increases the difference in CO₂ concentration between the on- and off-branch (green lines Fig. 3b). The climate sensitivity coupling increases this effect, with a larger effect for the higher climate sensitivity (purple and red lines Fig. 3d). In the cases using the rain ratio, the potential of the E_s-coupling becomes visible. In these cases, atmospheric pCO₂ values deviate more from pCO_{2,0} and therefore have a larger effect on E_s. When E_s differs from the default value (0.39 Sv), both saddle nodes move to different E_a values.

To explain the movement of the saddle nodes, we consider the sensitivity of the model to E_s (Fig. 4). In Fig. 4 the location of the saddle nodes on both the on- and the off-branch are shown versus the value of E_s. This figure shows that as E_s increases, the MEW also increases. The default value used for cases REF and BIO for E_s is 0.39 Sv. The CMIP6 CO₂-dependent fit (8) results in a slightly smaller value. Due to decreased E_s, the thermocline becomes fresher, and in combination with the salt-advection feedback, this leads to a smaller meridional density gradient and therefore a weaker AMOC. Furthermore, decreased E_s decreases the net evaporation over the Atlantic, given by (E_s-E_a) and this means that a smaller E_a is necessary to tip the AMOC. On the off-branch, a smaller E_s results in salinification of the *ts* box and a less negative freshwater flux (E_a) is needed to decrease the meridional density gradient and reinvigorate the AMOC. For cases with the FCA feedback, it reduces the MEW by moving the off-branch saddle node to larger values of E_a, and the saddle node on the on-branch to smaller values, which can be explained by the fact that CO₂ is smaller than CO_{2,0} and therefore E_s is smaller than E_{s,base} in (8).

In the bifurcation diagrams in Fig. 3 we find that the solution on the on-branch becomes unstable before passing the saddle node. This change in stability can be explained by the presence of a subcritical Hopf bifurcation in the circulation model. The internal oscillation corresponding to this Hopf bifurcation is unstable and has a multidecadal periodicity. In this study we are only interested in the MEW of the AMOC, and we therefore do not consider the Hopf bifurcation further.

3.3 Sensitivity to total carbon content

Over the Cenozoic, both the AMOC (Lynch-Stieglitz, 2017) and total carbon content in the ocean-atmosphere system have varied (Zeebe et al., 2009; Caves et al., 2016). In Caves et al. (2016) it is suggested that total carbon content has varied between 24,000 PgC and 96,000 PgC. In the previous section, the model was studied with approximately 40,000 PgC in the global system. In this section, we analyze how the sensitivity of the AMOC MEW changes under different total carbon contents in the model. To test the sensitivity, we remove approximately 4,000 (-10%) PgC, and add approximately 4,000 (+10%), 10,000 (+25%) and 20,000 (+50%) PgC. We do this for the cases considered in Section 3.2 excluding case REF (Fig. 5).

In case BIO there is no change in the MEW, which is to be expected since there is no back coupling from the carbon cycle model to the AMOC model, and the AMOC solution is therefore independent of the carbon cycle. We see only the effect of total carbon content on atmospheric pCO₂ values. When carbon is removed, the CO₂ concentrations at the saddle nodes both decrease. However, when carbon is added, only the saddle node on the on-branch has higher CO₂ concentrations, independent of whether 4,000, 10,000 or 20,000 PgC is added. We see a similar pattern for the E_s + BIO case, but here the MEW increases for larger total carbon content due to the different CO₂ concentrations at the saddle nodes. The cases including the rain ratio

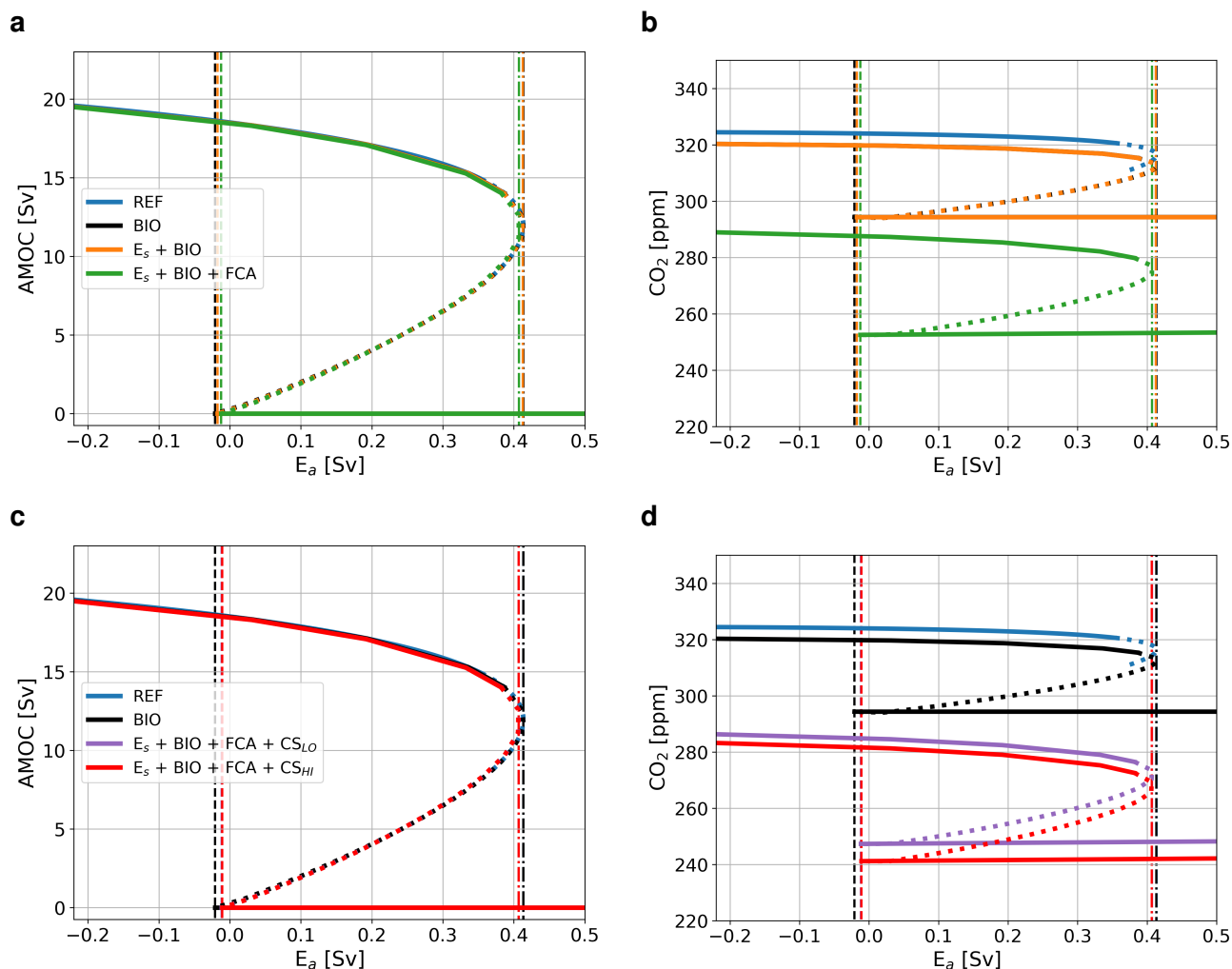


Figure 3. Bifurcation diagram showing the sensitivity of the AMOC and atmospheric pCO_2 to E_a . Solid lines represent stable steady state solutions, dotted lines represent unstable solutions, dash-dotted lines represent the location of the saddle node on the on-branch, and dashed lines the location of the saddle node on the off-branch. The blue lines represent a case without additional coupling (REF), the black lines with only the biological coupling (BIO), the orange lines with the CMIP6 based E_s and biological coupling ($E_s + \text{BIO}$), and the green lines represent a case where also the rain ratio feedback is applied ($E_s + \text{BIO} + \text{FCA}$). The purple and red lines also include the climate sensitivity feedback, where purple lines represent a low sensitivity ($E_s + \text{BIO} + \text{FCA} + CS_{LO}$) and red lines a high sensitivity, ($E_s + \text{BIO} + \text{FCA} + CS_{HI}$). Results are for the AMOC strength in Sv (a, c) and atmospheric pCO_2 in ppm (b, d). Especially for the AMOC strength results are very similar and overlap in the plots. In (b) the black curve (BIO) is under the orange curve ($E_s + \text{BIO}$).

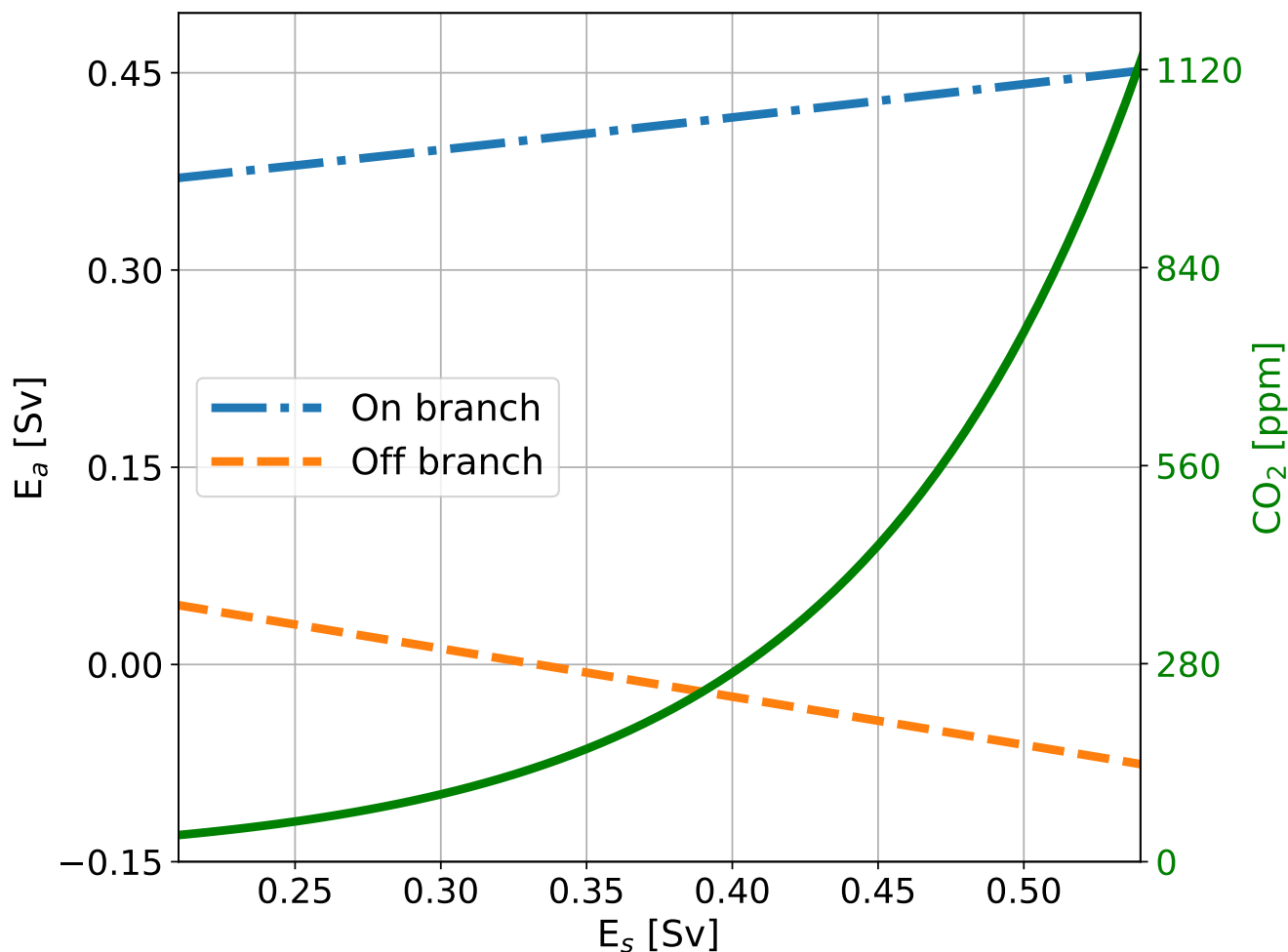


Figure 4. E_a -value corresponding to the saddle node on the on-branch (dash-dotted blue line, left y-axis) and the off-branch (dashed orange line, left y-axis) for different values of E_s in Sv. The green line (right y-axis) represent the CO_2 values corresponding to the E_s -values following the used fit (8).

feedback show a different pattern. Here, the CO_2 concentrations at both saddle nodes are dependent on the amount of carbon added to the ocean-atmosphere system, i.e. the higher the content, the higher the CO_2 concentrations at the saddle nodes (Fig. 5b). This influences the value of E_s at the saddle nodes (Fig. 5c), which increases the MEW for increasing carbon content (Fig. 5a). The MEW shift increases when the climate sensitivity coupling is used (CS_{Lo} and CS_{Hi}), with a larger response for the higher sensitivity (CS_{Hi}). Another effect visible in the cases using the FCA feedback is the difference in CO_2 concentration between the on- and the off-branch increases as total carbon content increases. This effect is larger when climate sensitivity is increased.

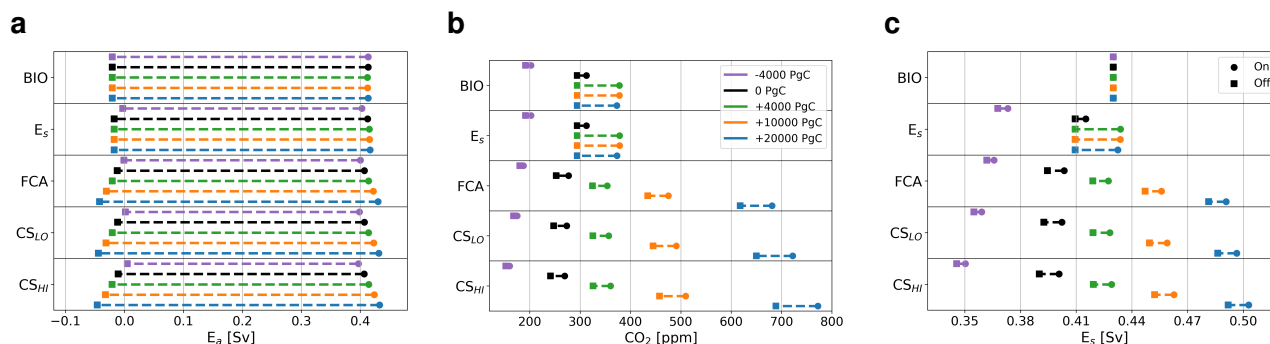


Figure 5. Panel a shows the location of the saddle nodes versus E_a in Sv, panel b shows the corresponding CO_2 concentration in ppm, and c shows the corresponding value of E_s in Sv. The top row of the figure represents case BIO, the second row case $E_s + BIO$, and the middle row case $E_s + BIO + FCA$, the fourth row case $E_s + BIO + FCA + CS_{LO}$, and the bottom row $E_s + BIO + FCA + CS_{HI}$. Square markers represent the location of the saddle node on the off-branch and round markers the location of the saddle node on the on-branch for cases where 4000 PgC is removed (purple), the default carbon content (black), 4000 PgC is added (green), 10,000 PgC is added (orange) and where 20,000 PgC is added (blue).

We can explain the behavior of the MEW in the $E_s + BIO$ case by looking at the atmospheric pCO_2 values, and therefore also E_s , at the saddle nodes, which are similar for the three high total carbon cases. However, when the rain ratio feedback is used, we see that the MEW keeps increasing for larger carbon contents since also the atmospheric pCO_2 increases. We can explain the difference between $E_s + BIO$ and the cases where the rain ratio feedback is used by the constraint on total carbon in the ocean-atmosphere system. In $E_s + BIO$, biological export production in the Atlantic is mainly a function of the AMOC strength, whereas in the $E_s + BIO + FCA$ case it is also dependent on the $CaCO_3$ saturation state which is coupled to atmospheric pCO_2 through the pH of the surface ocean. This leads to a larger outflux of DIC and Alk to the sediments, which, in steady state, needs to be balanced by a higher influx of DIC and Alk through the river flux, which can only be achieved by increasing atmospheric pCO_2 .

A second result for the cases with the rain ratio feedback is that the CO_2 concentration difference between the on- and off-branch increases for higher total carbon content. As we increase total carbon content in the system, the rain ratio increases on both the on- and the off-branch because the saturation state of $CaCO_3$ increases. Due to non-linearities in the carbonate chemistry, the more carbon is present in the system, the larger the difference in rain ratio between the two branches. This explains why the difference between the on- and off-branch increases as total carbon content increases in the system.

4 Summary and discussion

In this paper we investigated the multiple equilibria window (MEW) of the AMOC in a coupled ocean circulation-carbon cycle box model. When freshwater forcing is coupled to atmospheric pCO_2 using a CMIP6 multi-model fit equation (8) above, the



285 MEW changes slightly due to a dependency on atmospheric $p\text{CO}_2$. We also assessed the sensitivity to total carbon content in
the system and found that the MEW is larger with more carbon in the system due to a shift of both the on- and off-branch
saddle nodes. These results show the potential of the marine carbon cycle to influence the MEW of the AMOC.

We acknowledge that it is difficult to assess the validity of the CMIP6 E_s - $p\text{CO}_2$ fit since that fit is based on a transient
simulation with a strong forcing. However, longer (i.e. more than 3000 year) simulations by Galbraith and de Lavergne (2019)
290 show a similar, slightly stronger relation than the one used in this study. These clear and plausible mechanisms are more
important than the precise quantitative estimates and are summarized in Fig. 6. Two processes explain the results on the MEW:
(1) the balance between the river flux and sediment flux that constrains atmospheric $p\text{CO}_2$ (first two panels in Fig. 6a, b); and
(2) the sensitivity of the AMOC to E_s (last panel in Fig. 6a, b). In the model, atmospheric $p\text{CO}_2$ is dependent on the ocean
circulation through the effect of export production on the burial of DIC and Alk in the sediments. In steady state, this burial
295 needs to balance the riverine influx which is dependent on atmospheric $p\text{CO}_2$. When the E_s -coupling is used, E_s is dependent
on atmospheric $p\text{CO}_2$, and the ocean circulation is dependent on E_s , creating a feedback loop (Fig. 6). If the CO_2 concentration
in the atmosphere is larger than $\text{CO}_{2,0}$, the MEW increases, while it decreases if it is smaller than $\text{CO}_{2,0}$. This results in that
when atmospheric $p\text{CO}_2$ is high, so is E_s which results in a stronger AMOC on the on-branch. As a consequence, export
production is increased and there will be a larger outflux of carbon and alkalinity through the sediments, which is balanced
300 by a high influx of carbon through the rivers, consistent with high atmospheric $p\text{CO}_2$ values. Of the feedbacks that we have
implemented, only the rain ratio feedback (FCA) affects this mechanism because it directly influences the sediment outflux
and makes the carbon cycle less sensitive to the ocean circulation.

The results here can be relevant when studying climate transitions in past and future climates as mechanisms how AMOC
stability can depend on background climate and atmospheric $p\text{CO}_2$ values are identified. Previous work focused on the Pleis-
305 tocene suggest an influence of atmospheric $p\text{CO}_2$ on the stability structure of the AMOC through temperature (Sun et al.,
2022) and moisture transport (Zhang et al., 2017). In our model, there is no direct effect of temperature changes on the AMOC
strength, but the E_s -coupling used here is similar to the moisture transport described in Zhang et al. (2017). The only difference
is that this moisture transport is directly to the Pacific basin in their study, whereas in our model we rescale freshwater fluxes
to set this direct flux to 0.

310 We have used a model that provides a simple framework for studying AMOC dynamics that allows us to efficiently test the
concept of AMOC stability in a wide range of parameter values. However, a limitation is that in the model temperature is not
a state variable, based on the assumption that the timescales of salinity variations is longer than that of temperature and thus
dominant in steady state. This means that the AMOC strength in our model is not influenced by changes in temperature, which
is a caveat of this study. Under high carbon content in the ocean-atmosphere system, this might not be valid. However, we also
315 have explored also relatively small changes in the total carbon content and the mechanisms presented here are also valid for
this smaller range, suggesting that the main mechanism presented in this study is at least valid for small changes in the total
carbon content. We do not expect that the MEW shift described in this study is fully compensated for when temperature is a
state variable. Though not a limitation in the model, it is good to note that the range of timescales in the carbon cycle model



is larger than in the circulation model, which does not affect our results but does affect the time dependent response of the
320 system.

Our work also holds implications for assessing AMOC stability in future climates. Currently, the global warming threshold
for an AMOC collapse is estimated to be 4 °C (Armstrong-McKay et al., 2022). In the future, the carbon content of the ocean-
atmosphere system will increase, potentially increasing the MEW which can change the likelihood of a bifurcation induced
AMOC collapse. In this study we focused on slow, bifurcation induced tipping of the AMOC, while the AMOC is also able to
325 tip due to faster processes (e.g. density changes related to temperature variations) resulting in noise-induced tipping (Castellana
et al., 2019; Jacques-Dumas et al., 2023). The mechanisms presented here might influence these noise-induced transitions as
well. We hope this work inspires further research on the dependency of the AMOC MEW on the carbon cycle in more detailed
models, to further investigate the relevance of the mechanism found in this study, and provide a better quantification for the
influence of the marine carbon cycle on the MEW of the AMOC.

330 *Code and data availability.* All model code, data and scripts are available at <https://doi.org/10.5281/zenodo.10005999> (Boot et al., 2023).
AUTO-07p can be downloaded from <https://github.com/auto-07p/auto-07p> (Doedel, E J and Paffenroth, R C and Champneys, A C and
Fairgrieve, T F and Kuznetsov, Yu A and Oldeman, B E and Sandstede, B and Wang, X J, 2021).

Appendix A: Additional couplings, feedbacks and simulations

Besides the couplings and feedbacks presented in the main text we have introduced one additional coupling and two additional
335 feedbacks to the carbon cycle. A summary of these cases and the results can be seen in Table A1 and Fig. A1. The main effects
of these additional coupling and feedbacks is a shift in atmospheric pCO₂ values on the on-branch for cases with the piston
velocity feedback (Eq. A3 and Eq. A4). This shift is larger when also the climate sensitivity feedback is used. A description of
the additional coupling and feedbacks is given below.

The additional coupling we have introduced is the addition of dilution fluxes for both DIC and Alk related to the freshwater
340 fluxes E_s and E_a (Eq. A1). Increasing the concentrations of DIC and Alk due to evaporation and decreasing the concentrations
due to a net influx of freshwater at the surface.

$$C_{dil,i} = \lambda_D \times (E_s + E_a) \times \frac{C_i}{V_i} \quad (A1)$$

Where C_i is the tracer concentration in box i and V_i the volume, and λ_D is a parameter that determines whether the coupling
is used ($\lambda_D = 1$) or not ($\lambda_D = 0$). The dilutive fluxes for Alk are modelled in a similar fashion.

345 A first additional feedback we introduce is a linear temperature dependency in the biological efficiency (Eq. A2) which was
introduced in the biological coupling. Under an SST increase, the efficiency will decrease following



Table A1. Additional cases not included in the main text using additional feedbacks as described in this document. Results of these cases can be seen in Fig. A1.

Notation	S-1	S-2	S-3	S-4	S-5	S-6	S-7	S-8	S-9	S-10
λ_{BI}	1	1	1	1	1	1	1	1	1	1
λ_T	1	0	0	1	1	1	0	0	1	1
λ_P	0	0	1	1	1	0	0	1	1	1
λ_D	0	1	0	0	0	0	1	0	0	0
λ_ϵ	0	0	0	0	1	0	0	0	0	1
λ_E	0	0	0	0	0	1	1	1	1	1

$$\epsilon_i = (\lambda_\epsilon \times -0.1\Delta T) + \epsilon_{i,base} \quad (\text{A2})$$

For this feedback it is necessary to also use the climate sensitivity feedback and the strength can be regulated with λ_ϵ .

The second additional feedback allows the piston velocity (k_w) to vary with the SSTs (Eq. A3). When the climate sensitivity feedback is used, this also affects the piston velocity. The temperature dependency is introduced by making the piston velocity a function of the Schmidt number (Eq. A4) following

$$k_{w,i} = (1 - \lambda_P) \times k_{w,ibase} + \lambda_P k_{w,ibase} \times \left(\frac{Sc_i}{660}\right)^{-0.5} \quad (\text{A3})$$

Where

$$Sc_i = 2116.8 - 136.25T_i + 4.7353T_i^2 - 0.092307T_i^3 + 0.0007555T_i^4 \quad (\text{A4})$$

In this case the feedback can either be switched on ($\lambda_P = 1$) or off ($\lambda_P = 0$). Without this feedback the piston velocity is similar for all boxes, but with this feedback the piston velocity will differ per box.

Appendix B: Model parameters

The model parameters are presented in Tables B3 to B5.

Appendix C: Model equations

There are in total 30 state variables: salinity, DIC, alkalinity, and PO_4 in the 7 boxes, the pycnocline depth D, and atmospheric pCO_2 . The state variables in the deep Atlantic box are determined using conservation laws. The salinity equations are given by Eq. C1-C6, the conservation of salt in the model is given by Eq. C8, and the pycnocline depth is determined using Eq. C7. The volume fluxes are determined using Eq. C9 to C13, and the equation of state is given by Eq. C14. The equations for the carbon cycle model are given by Eq. C15 to Eq. C27.



Table B1. Symbol (column 1), description (column 2), value (column 3), and units (column 4) of the general parameters used in the ocean circulation model based on (Cimatoribus et al., 2014).

Symbol	Description	Value	Units
$V_{0,A}$	Total volume of the Atlantic basin	3×10^{17}	m^3
V_n	Volume of box n	3×10^{15}	m^3
V_s	Volume of box s	9×10^{15}	m^3
A_t	Surface area box t	1×10^{14}	m^2
L_{xA}	Zonal extent of the Atlantic Ocean at its southern end	1×10^7	m
L_y	Meridional extent of the frontal region of the Southern Ocean	1×10^6	m
L_{xS}	Zonal extent of the Southern Ocean	3×10^7	m
τ	Average zonal wind stress amplitude	0.1	N m^{-2}
A_{GM}	Eddy diffusivity	1700	$\text{m}^2 \text{s}^{-1}$
f_S	Coriolis parameter	-1×10^{-4}	s^{-1}
ρ_0	Reference density	1027.5	kg m^{-3}
κ	Vertical diffusivity	1×10^{-5}	$\text{m}^2 \text{s}^{-1}$
S_0	Reference salinity	35	g/kg
T_0	Reference temperature	5	$^\circ\text{C}$
$T_{n,base}$	Base temperature box n	5	$^\circ\text{C}$
$T_{ts,base}$	Base temperature box ts	10	$^\circ\text{C}$
η	Hydraulic constant	3×10^4	m s^{-1}
α	Thermal expansion coefficient	2×10^{-4}	K^{-1}
β	Haline contraction coefficient	8×10^{-4}	$(\text{g/kg})^{-1}$
r_S	Transport by the southern subtropical gyre	10×10^6	$\text{m}^3 \text{s}^{-1}$
r_N	Transport by the northern subtropical gyre	5×10^6	$\text{m}^3 \text{s}^{-1}$

$$365 \quad \frac{d(V_t S_t)}{dt} = q_S(\theta(q_S)S_{ts} + \theta(-q_S)S_t + q_U S_d - \theta(q_N)q_N S_t + r_s(S_{ts} - S_t) + r_N(S_n - S_t) + 2E_s S_0 \quad (\text{C1})$$

$$\frac{d(V_{ts} S_{ts})}{dt} = q_{Ek} S_s - q_e S_{ts} - q_S(\theta(q_S)S_{ts} + \theta(-q_S)S_t) + r_S(S_t - S_{ts}) \quad (\text{C2})$$

$$V_n \frac{dS_n}{dt} = \theta(q_N)q_N(S_t - S_n) + r_N(S_t - S_n) - (E_s + E_a)S_0 \quad (\text{C3})$$

$$V_s \frac{dS_s}{dt} = q_S(\theta(q_S)S_d + \theta(-q_S)S_s) + q_e S_{ts} - q_{Ek} S_s - (E_p + E_s - E_a)S_0 + (r_P + \psi_1)(S_{ps} - S_s) \quad (\text{C4})$$



Table B2. Symbol (column 1), description (column 2), value (column 3), and units (column 4) of the general parameters used in the ocean circulation model added or changed with respect to (Cimatoribus et al., 2014)

Symbol	Description	Value	Units
E_s	Symmetric freshwater flux	0.39×10^6	$\text{m}^3 \text{s}^{-1}$
E_p	Freshwater flux from box ps to box s	0.99×10^6	$\text{m}^3 \text{s}^{-1}$
V_0	Total volume of the ocean	1.5×10^{18}	m^3
V_{ps}	Volume Box ps	9×10^{16}	m^3
V_{pd}	Volume Box pd	1.11×10^{18}	m^3
d_{ps}	Depth Box ps	300	m
d_{fn}	Floor depth Box n	300	m
d_{ft}	Floor depth Box t	variable (D)	m
d_{fts}	Floor depth Box ts	variable (D)	m
d_{fs}	Floor depth Box s	300	m
d_{fd}	Floor depth Box d	4000	m
$T_{t,base}$	Base temperature Box t	23.44	$^{\circ}\text{C}$
$T_{s,base}$	Base temperature Box s	0.93	$^{\circ}\text{C}$
T_d	Temperature Box d	1.8	$^{\circ}\text{C}$
T_{ps}	Temperature Box ps	23.44	$^{\circ}\text{C}$
T_{pd}	Temperature Box pd	1.8	$^{\circ}\text{C}$
r_P	Transport by the subtropical gyre between box s and ps	90×10^6	$\text{m}^3 \text{s}^{-1}$

$$V_{ps} \frac{dS_{ps}}{dt} = (\gamma_1 + \psi_1) * (S_{pd} - S_{ps}) + (r_P * (S_s - S_{ps})) + E_p \quad (\text{C5})$$

$$370 \quad V_{pd} \frac{dS_{pd}}{dt} = \gamma_1 * (S_{ps} - S_{pd}) + \psi_1 (S_d - S_{pd}) \quad (\text{C6})$$

$$\left(A + \frac{L_x A L_y}{2}\right) \frac{dD}{dt} = q_U + q_{Ek} - q_e - \theta(q_N)q_N \quad (\text{C7})$$

$$S_0 V_0 = V_n S_n + V_d S_d + V_t S_t + V_{ts} S_{ts} + V_s S_s + V_{ps} S_{ps} + V_{pd} + S_{pd} \quad (\text{C8})$$

Where θ is a step function which takes a value of 1 for a positive argument, and takes a value of 0 for a negative argument. The volume fluxes are given by:



Table B3. Symbol (column 1), description (column 2), value (column 3), and units (column 4) of the general parameters used in the carbon cycle model based on (Boot et al., 2022).

Symbol	Description	Value	Units
V_{at}	Volume of the atmosphere	1.76×10^{20}	m^3
ψ_1	Global overturning circulation	18×10^6	$\text{m}^3 \text{s}^{-1}$
γ_1	Bidirectional mixing term between box ps and pd	30×10^6	$\text{m}^3 \text{s}^{-1}$
n	Order of CaCO_3 dissolution kinetics	1	-
P_C	Mass percentage of C in CaCO_3	0.12	-
D_{Ca}	Constant dissolution rate of CaCO_3	2.75×10^{-13}	$\text{mol m}^{-3} \text{s}^{-1}$
W_{SC}	Constant silicate weathering	2.4×10^{-12}	$\text{mol m}^{-3} \text{s}^{-1}$
W_{SV}	Variable silicate weathering parameter	1.6×10^{-8}	$\text{mol m}^{-3} \text{atm}^{-1} \text{s}^{-1}$
W_{CV}	Variable carbonate weathering parameter	6.3×10^{-8}	$\text{mol m}^{-3} \text{atm}^{-1} \text{s}^{-1}$
k_{Ca}	Constant CaCO_3 dissolution rate	4.4×10^{-6}	s^{-1}
b	Exponent in Martin's law	0.75	-
d_0	Reference depth for biological productivity	100	m
$k_{w,base}$	Base piston velocity	3	m/day
$R_{C:P}$	Redfield C:P ratio	130	mol C/mol P
$R_{P:C}$	Redfield P:C ratio	1/130	mol P/mol C
$[Ca]_n$	Calcium concentration Box n	$0.01028 \times S_n$	mol m^{-3}
$[Ca]_t$	Calcium concentration Box t	$0.01028 \times S_t$	mol m^{-3}
$[Ca]_{ts}$	Calcium concentration Box ts	$0.01028 \times S_{ts}$	mol m^{-3}
$[Ca]_s$	Calcium concentration Box s	$0.01028 \times S_s$	mol m^{-3}
$[Ca]_d$	Calcium concentration Box d	$0.01028 \times S_d$	mol m^{-3}

$$375 \quad q_{Ek} = \frac{\tau L_x S}{\rho_0 |f_S|} \quad (\text{C9})$$

$$q_e = A_{GM} \frac{L_x A}{L_y} D \quad (\text{C10})$$

$$q_U = \frac{\kappa A}{D} \quad (\text{C11})$$

$$q_N = \eta \frac{\rho_n - \rho_{ts}}{\rho_0} D^2 \quad (\text{C12})$$



Table B4. Symbol (column 1), description (column 2), value (column 3), and units (column 4) of the parameters used in the carbon cycle model that have been changed compared to (Boot et al., 2022).

Symbol	Description	Value	Units
$Z_{n,base}$	Base biological production Box n	1.9	$\text{mol C m}^{-2} \text{ yr}^{-1}$
$Z_{t,base}$	Base biological production Box t	2.1	$\text{mol C m}^{-2} \text{ yr}^{-1}$
$Z_{ts,base}$	Base biological production Box ts	2.1	$\text{mol C m}^{-2} \text{ yr}^{-1}$
$Z_{s,base}$	Base biological production Box s	1.1	$\text{mol C m}^{-2} \text{ yr}^{-1}$
$\epsilon_{n,base}$	Base biological efficiency Box n	0.1	-
$\epsilon_{t,base}$	Base biological efficiency Box t	0.5	-
$\epsilon_{ts,base}$	Base biological efficiency Box ts	0.3	-
$\epsilon_{s,base}$	Base biological efficiency Box s	0.1	-
$F_{Ca,base}$	Base rain ratio	0.15	-
$pCO_{2,0}$	Base atmospheric pCO_2 value	320	ppm

Table B5. The symbols and description of the equilibrium constants are presented in the first two columns. The third column presents the source of the used expression.

Symbol	Description	Expression
K_0	Solubility constant	Weiss (1974)
K_1	First dissociation constant of carbonic acid	Lueker et al. (2000)
K_2	Second dissociation constant of carbonic acid	Lueker et al. (2000)
$K_{sp,base}$	Equilibrium constant for $CaCO_3$ dissolution	Mucci (1983)
$\bar{K}_{sp,pres}$	Pressure correction for $K_{sp,base}$	Millero (1983)

$$380 \quad q_S = q_{Ek} - q_e \quad (C13)$$

$$\rho_i = \rho_0(1 - \alpha(T_i - T_0) + \beta(S_i - S_0)) \quad (C14)$$

Where i represents any box.

The carbon cycle equations are given by Eq. C15 to Eq. C19. The different fluxes are determined using Eq. C20 to Eq. C27.

$$\frac{d[DIC]_i}{dt} = C_{phys,i} + C_{bio,i} + C_{carb,i} + C_{air,i} + C_{river,t} \quad (C15)$$

$$385 \quad \frac{d[Alk]_i}{dt} = A_{phys,i} + A_{carb,i} + A_{river,t} \quad (C16)$$



$$\frac{d[PO_4^{3-}]_i}{dt} = P_{phys,i} + P_{bio,i} + P_{river,t} \quad (C17)$$

$$\frac{dC_{tot}}{dt} = C_{river,t} \times V_t + \sum_{i=1}^5 (C_{carb,i} V_i) + \sum_{i=1}^5 (C_{bio,i} V_i) \quad (C18)$$

$$\frac{dAlk_{tot}}{dt} = Alk_{river,t} \times V_t + Alk_{river,ps} \times V_{ps} + \sum_{i=1}^7 (Alk_{carb,i} V_i) \quad (C19)$$

In these equations the different terms represent advective fluxes (X_{phys}), biological fluxes (X_{bio}), carbonate fluxes (X_{carb}),
 390 air-sea gas exchange (C_{air}) and the river influx (X_{river}). From these fluxes, C_{air} only acts on the surface boxes, and X_{river}
 only on box t and box ps . X_{phys} is determined following:

$$X_{phys,i} = \frac{1}{V_i} \left(\sum_{i=1} (q_{j \rightarrow i} \times X_j) - \sum_{i=1} (q_{i \rightarrow j} \times X_i) \right) \quad (C20)$$

This equation represents that the concentration of tracer X changes through an advective flux flowing out of box i to box j
 ($q_{i \rightarrow j}$ times the concentration in box i (X_i), and a flux flowing into box i from box j ($q_{j \rightarrow i}$) times the concentration in box j
 395 (X_j). There can be fluxes from multiple boxes into one box.

$$C_{air,i} = \frac{K_{0,i} \times k_{w,i} \times \rho_0 \times (CO_2^{atm} - pCO_{2,i})}{V_i} \quad (C21)$$

For i is n , t , ts , s or ps . K_0 is the solubility constant, k_w the piston velocity, CO_2^{atm} the atmospheric CO_2 concentration, pCO_2
 the partial pressure of CO_2 in the ocean and V the volume of the ocean box.

$$C_{carb,i} = -\frac{Z_i \times A_i \times F_{Ca,i}}{V_i} + ([CO_3^{2-}]_i [Ca^{2+}]_i) \rho_0 k_{Ca} \left(1 - \frac{([CO_3^{2-}]_i [Ca^{2+}]_i)}{K_{sp,i}} \right)^n \times PerC + DC \quad (C22)$$

400 For i is n , t , ts , s or ps . Z represent biological production, A the surface area of the box, F_{Ca} the rain ratio and V the volume.
 Other variables are the carbonate ion concentration ($[CO_3^{2-}]$), calcium concentration ($[Ca^{2+}]$), and equilibrium constant for
 $CaCO_3$ dissolution (K_{sp}).

For box pd the carbonate flux is determined following

$$C_{carb,i} = ([CO_3^{2-}]_{pd} [Ca^{2+}]_{pd}) \rho_0 k_{Ca} \left(1 - \frac{([CO_3^{2-}]_{pd} [Ca^{2+}]_{pd})}{K_{sp,pd}} \right)^n \times PerC + ([CO_3^{2-}]_{pd} [Ca^{2+}]_{pd}) \rho_0 k_{Ca} \times \left(1 - \frac{([CO_3^{2-}]_{pd} [Ca^{2+}]_{pd})}{K_{sp, sed}} \right)^n \times PerC + DC \quad (C23)$$



405 Where there is a distinction between water column dissolution of CaCO_3 and dissolution in the sediments.

The biological fluxes in the surface ocean are given by:

$$C_{bio,i} = \frac{Z_i \times A_i}{V_i} \times \left(\frac{d_{fi}}{d_0}\right)^{-b} \quad (\text{C24})$$

For i is n , t , ts , s or ps . Z represent biological production, A the surface area of the box, V the volume, and d_{fi} the floor depth of the box.

410 The biological flux for box pd is given by:

$$C_{bio,i} = \frac{Z_{ps} \times A_{ps}}{V_{ps}} \times \left(\left(\frac{d_{fps}}{d_0}\right)^{-b} - \left(\frac{d_{tot}}{d_0}\right)^{-b}\right) \quad (\text{C25})$$

Alkalinity and phosphate fluxes are proportionate to DIC fluxes following:

$$A_{carb,i} = 2 \times C_{carb,i} \quad (\text{C26})$$

$$P_{bio,i} = r_{P:C} \times C_{bio,i} \quad (\text{C27})$$

415 Where $r_{P:C}$ is a constant stoichiometric P to C parameter.

An explanation and the value of all parameters are given in the tables in Appendix B.

Author contributions. AB constructed the AUTO version of the coupled model and obtained and analyzed the results. All authors contributed to the writing of the paper.

Competing interests. The authors declare that they have no conflict of interest.

420 *Financial support.* This research has been supported by the Netherlands Earth System Science Centre (grant no. 024.002.001)



References

- Andersson, A., Graw, K., Schröder, M., Fennig, K., Liman, J., Bakan, S., Hollmann, R., and Klepp, C.: Hamburg Ocean Atmosphere Parameters and Fluxes from Satellite Data - HOAPS 4.0, https://doi.org/10.5676/EUM_SAF_CM/HOAPS/V002, 2017.
- 425 Armstrong-McKay, D. I., Staal, A., Abrams, J. F., Winkelmann, R., Sakschewski, B., Loriani, S., Fetzer, I., Cornell, S. E., Rockström, J., and Lenton, T. M.: Exceeding 1.5°C global warming could trigger multiple climate tipping points, *Science*, 377, eabn7950, <https://doi.org/10.1126/science.abn7950>, 2022.
- Barker, S. and Knorr, G.: Millennial scale feedbacks determine the shape and rapidity of glacial termination, *Nature Communications*, 12, 2273, <https://doi.org/10.1038/s41467-021-22388-6>, 2021.
- 430 Barker, S., Knorr, G., Vautravers, M. J., Diz, P., and Skinner, L. C.: Extreme deepening of the Atlantic overturning circulation during deglaciation, *Nature Geoscience*, 3, 567–571, <https://doi.org/10.1038/ngeo921>, 2010.
- Barker, S., Chen, J., Gong, X., Jonkers, L., Knorr, G., and Thornalley, D.: Icebergs not the trigger for North Atlantic cold events, *Nature*, 520, 333–336, <https://doi.org/10.1038/nature14330>, 2015.
- Bauska, T. K., Marcott, S. A., and Brook, E. J.: Abrupt changes in the global carbon cycle during the last glacial period, *Nature Geoscience*, 435 14, 91–96, <https://doi.org/10.1038/s41561-020-00680-2>, 2021.
- Boot, A., von der Heydt, A. S., and Dijkstra, H. A.: Effect of the Atlantic Meridional Overturning Circulation on atmospheric CO_2 variations, *Earth System Dynamics*, 13, 1041–1058, <https://doi.org/10.5194/esd-13-1041-2022>, 2022.
- Boot, A. A., von der Heydt, A. S., and Dijkstra, H. A.: ESD AABOOT AMOC MEW, <https://doi.org/https://doi.org/10.5281/zenodo.10005999>, 2023.
- 440 Castellana, D., Baars, S., Wubs, F. W., and Dijkstra, H. A.: Transition Probabilities of Noise-induced Transitions of the Atlantic Ocean Circulation, *Scientific Reports*, 9, 20284, <https://doi.org/10.1038/s41598-019-56435-6>, 2019.
- Caves, J. K., Jost, A. B., Lau, K. V., and Maher, K.: Cenozoic carbon cycle imbalances and a variable weathering feedback, *Earth and Planetary Science Letters*, 450, 152–163, <https://doi.org/https://doi.org/10.1016/j.epsl.2016.06.035>, 2016.
- Cimatoribus, A. A., Drijfhout, S. S., and Dijkstra, H. A.: Meridional overturning circulation: stability and ocean feedbacks in a box model, 445 *Climate Dynamics*, 42, 311–328, <https://doi.org/10.1007/s00382-012-1576-9>, 2014.
- Dekker, M. M., von der Heydt, A. S., and Dijkstra, H. A.: Cascading transitions in the climate system, *Earth System Dynamics*, 9, 1243–1260, <https://doi.org/10.5194/esd-9-1243-2018>, 2018.
- Dey, D. and Döös, K.: Atmospheric Freshwater Transport From the Atlantic to the Pacific Ocean: A Lagrangian Analysis, *Geophysical Research Letters*, 47, e2019GL086176, <https://doi.org/https://doi.org/10.1029/2019GL086176>, 2020.
- 450 Dijkstra, H. A.: Characterization of the multiple equilibria regime in a global ocean model, *Tellus A*, 59, 695–705, <https://doi.org/https://doi.org/10.1111/j.1600-0870.2007.00267.x>, 2007.
- Doedel, E. J., Paffenroth, R. C., Champneys, A. C., Fairgrieve, T. F., Kuznetsov, Y. A., Oldeman, B. E., Sandstede, B., and Wang, X. J.: AUTO-07p: Continuation and Bifurcation Software for Ordinary Differential Equations, 2007.
- Doedel, E J and Paffenroth, R C and Champneys, A C and Fairgrieve, T F and Kuznetsov, Yu A and Oldeman, B E and Sandstede, B and 455 Wang, X J: auto-07p, <https://github.com/auto-07p/auto-07p>, 2021.
- Drijfhout, S.: Competition between global warming and an abrupt collapse of the AMOC in Earth’s energy imbalance, *Scientific Reports*, 5, 14877, <https://doi.org/10.1038/srep14877>, 2015.



- Eyring, V., Bony, S., Meehl, G. A., Senior, C. A., Stevens, B., Stouffer, R. J., and Taylor, K. E.: Overview of the Coupled Model Intercomparison Project Phase 6 (CMIP6) experimental design and organization, *Geosci. Model Dev.*, 9, 1937–1958, <https://doi.org/10.5194/gmd-9-1937-2016>, 2016.
- Follows, M. J., Ito, T., and Dutkiewicz, S.: On the solution of the carbonate chemistry system in ocean biogeochemistry models, *Ocean Modelling*, 12, 290–301, <https://doi.org/https://doi.org/10.1016/j.ocemod.2005.05.004>, 2006.
- Galbraith, E. and de Lavergne, C.: Response of a comprehensive climate model to a broad range of external forcings: relevance for deep ocean ventilation and the development of late Cenozoic ice ages, *Climate Dynamics*, 52, 653–679, <https://doi.org/10.1007/s00382-018-4157-8>, 2019.
- Gottschalk, J., Battaglia, G., Fischer, H., Frölicher, T. L., Jaccard, S. L., Jeltsch-Thömmes, A., Joos, F., Köhler, P., Meissner, K. J., Menviel, L., Nehrass-Ahles, C., Schmitt, J., Schmittner, A., Skinner, L. C., and Stocker, T. F.: Mechanisms of millennial-scale atmospheric CO₂ change in numerical model simulations, *Quaternary Science Reviews*, 220, 30–74, <https://doi.org/https://doi.org/10.1016/j.quascirev.2019.05.013>, 2019.
- Jackson, L. C., Kahana, R., Graham, T., Ringer, M. A., Woollings, T., Mecking, J. V., and Wood, R. A.: Global and European climate impacts of a slowdown of the AMOC in a high resolution GCM, *Climate Dynamics*, 45, 3299–3316, <https://doi.org/10.1007/s00382-015-2540-2>, 2015.
- Jacques-Dumas, V., van Westen, R. M., Bouchet, F., and Dijkstra, H. A.: Data-driven methods to estimate the committor function in conceptual ocean models, *Nonlinear Processes in Geophysics*, 30, 195–216, <https://doi.org/10.5194/npg-30-195-2023>, 2023.
- Lenton, T. M., Held, H., Kriegler, E., Hall, J. W., Lucht, W., Rahmstorf, S., and Schellnhuber, H. J.: Tipping elements in the Earth’s climate system, *Proceedings of the National Academy of Sciences*, 105, 1786–1793, <https://doi.org/10.1073/pnas.0705414105>, 2008.
- Lueker, T. J., Dickson, A. G., and Keeling, C. D.: Ocean pCO₂ calculated from dissolved inorganic carbon, alkalinity, and equations for K₁ and K₂: validation based on laboratory measurements of CO₂ in gas and seawater at equilibrium, *Marine Chemistry*, 70, 105–119, [https://doi.org/https://doi.org/10.1016/S0304-4203\(00\)00022-0](https://doi.org/https://doi.org/10.1016/S0304-4203(00)00022-0), 2000.
- Lynch-Stieglitz, J.: The Atlantic Meridional Overturning Circulation and Abrupt Climate Change, *Annual Review of Marine Science*, 9, 83–104, <https://doi.org/10.1146/annurev-marine-010816-060415>, 2017.
- Marchal, O., Stocker, T. F., and Joos, F.: Impact of oceanic reorganizations on the ocean carbon cycle and atmospheric carbon dioxide content, *Paleoceanography*, 13, 225–244, <https://doi.org/https://doi.org/10.1029/98PA00726>, 1998.
- Martin, J. H., Knauer, G. A., Karl, D. M., and Broenkow, W. W.: VERTEX: carbon cycling in the northeast Pacific, *Deep Sea Research Part A. Oceanographic Research Papers*, 34, 267–285, [https://doi.org/https://doi.org/10.1016/0198-0149\(87\)90086-0](https://doi.org/https://doi.org/10.1016/0198-0149(87)90086-0), 1987.
- Matsumoto, K. and Yokoyama, Y.: Atmospheric $\Delta^{14}\text{C}$ reduction in simulations of Atlantic overturning circulation shutdown, *Global Biogeochemical Cycles*, 27, 296–304, <https://doi.org/https://doi.org/10.1002/gbc.20035>, 2013.
- Millero, F. J.: CHAPTER 43 - Influence of Pressure on Chemical Processes in the Sea, pp. 1–88, Academic Press, <https://doi.org/https://doi.org/10.1016/B978-0-12-588608-6.50007-9>, 1983.
- Mucci, A.: The solubility of calcite and aragonite in seawater at various salinities, temperatures, and one atmosphere total pressure, *American Journal of Science*, 283, 780–799, <https://doi.org/10.2475/ajs.283.7.780>, 1983.
- Munhoven, G.: Mathematics of the total alkalinity–pH equation - pathway to robust and universal solution algorithms: the SolveSAPHE package v1.0.1, *Geoscientific Model Development*, 6, 1367–1388, <https://doi.org/10.5194/gmd-6-1367-2013>, 2013.
- O’Neill, C. M., Hogg, A. M., Ellwood, M. J., Eggins, S. M., and Opdyke, B. N.: The [simple carbon project] model v1.0, *Geoscientific Model Development*, 12, 1541–1572, <https://doi.org/10.5194/gmd-12-1541-2019>, 2019.



- Palter, J. B.: The Role of the Gulf Stream in European Climate, *Annual Review of Marine Science*, 7, 113–137, <https://doi.org/10.1146/annurev-marine-010814-015656>, 2015.
- Rahmstorf, S.: Ocean circulation and climate during the past 120,000 years, *Nature*, 419, 207–214, <https://doi.org/10.1038/nature01090>, 2002.
- 500 Schmittner, A. and Galbraith, E. D.: Glacial greenhouse-gas fluctuations controlled by ocean circulation changes, *Nature*, 456, 373–376, <https://doi.org/10.1038/nature07531>, 2008.
- Sinet, S., von der Heydt, A. S., and Dijkstra, H. A.: AMOC Stabilization Under the Interaction With Tipping Polar Ice Sheets, *Geophysical Research Letters*, 50, e2022GL100305, <https://doi.org/https://doi.org/10.1029/2022GL100305>, 2023.
- Sun, Y., Knorr, G., Zhang, X., Tarasov, L., Barker, S., Werner, M., and Lohmann, G.: Ice sheet decline and rising at-
505 mospheric CO₂ control AMOC sensitivity to deglacial meltwater discharge, *Global and Planetary Change*, 210, 103755, <https://doi.org/https://doi.org/10.1016/j.gloplacha.2022.103755>, 2022.
- Vellinga, M. and Wood, R. A.: Global Climatic Impacts of a Collapse of the Atlantic Thermohaline Circulation, *Climatic Change*, 54, 251–267, <https://doi.org/10.1023/A:1016168827653>, 2002.
- Vellinga, M. and Wood, R. A.: Impacts of thermohaline circulation shutdown in the twenty-first century, *Climatic Change*, 91, 43–63,
510 <https://doi.org/10.1007/s10584-006-9146-y>, 2008.
- Weijer, W., Cheng, W., Drijfhout, S. S., Fedorov, A. V., Hu, A., Jackson, L. C., Liu, W., McDonagh, E. L., Mecking, J. V., and Zhang, J.: Stability of the Atlantic Meridional Overturning Circulation: A Review and Synthesis, *Journal of Geophysical Research: Oceans*, 124, 5336–5375, <https://doi.org/https://doi.org/10.1029/2019JC015083>, 2019.
- Weijer, W., Cheng, W., Garuba, O. A., Hu, A., and Nadiga, B. T.: CMIP6 Models Predict Significant 21st Cen-
515 tury Decline of the Atlantic Meridional Overturning Circulation, *Geophysical Research Letters*, 47, e2019GL086075, <https://doi.org/https://doi.org/10.1029/2019GL086075>, 2020.
- Weiss, R. F.: Carbon dioxide in water and seawater: the solubility of a non-ideal gas, *Marine Chemistry*, 2, 203–215, [https://doi.org/https://doi.org/10.1016/0304-4203\(74\)90015-2](https://doi.org/https://doi.org/10.1016/0304-4203(74)90015-2), 1974.
- Williams, R. G. and Follows, M. J.: *Ocean Dynamics and the Carbon Cycle: Principles and Mechanisms*, Cambridge University Press,
520 Cambridge, <https://doi.org/DOI:10.1017/CBO9780511977817>, 2011.
- Wood, R. A., Rodríguez, J. M., Smith, R. S., Jackson, L. C., and Hawkins, E.: Observable, low-order dynamical controls on thresholds of the Atlantic meridional overturning circulation, *Climate Dynamics*, 53, 6815–6834, <https://doi.org/10.1007/s00382-019-04956-1>, 2019.
- Wunderling, N., Donges, J. F., Kurths, J., and Winkelmann, R.: Interacting tipping elements increase risk of climate domino effects under global warming, *Earth System Dynamics*, 12, 601–619, <https://doi.org/10.5194/esd-12-601-2021>, 2021.
- 525 Zeebe, R. E., Zachos, J. C., and Dickens, G. R.: Carbon dioxide forcing alone insufficient to explain Palaeocene–Eocene Thermal Maximum warming, *Nature Geoscience*, 2, 576–580, <https://doi.org/10.1038/ngeo578>, 2009.
- Zelinka, M. D., Myers, T. A., McCoy, D. T., Po-Chedley, S., Caldwell, P. M., Ceppi, P., Klein, S. A., and Taylor, K. E.: Causes of Higher Climate Sensitivity in CMIP6 Models, *Geophysical Research Letters*, 47, e2019GL085782, <https://doi.org/https://doi.org/10.1029/2019GL085782>, 2020.
- 530 Zhang, X., Knorr, G., Lohmann, G., and Barker, S.: Abrupt North Atlantic circulation changes in response to gradual CO₂ forcing in a glacial climate state, *Nature Geoscience*, 10, 518–523, <https://doi.org/10.1038/ngeo2974>, 2017.

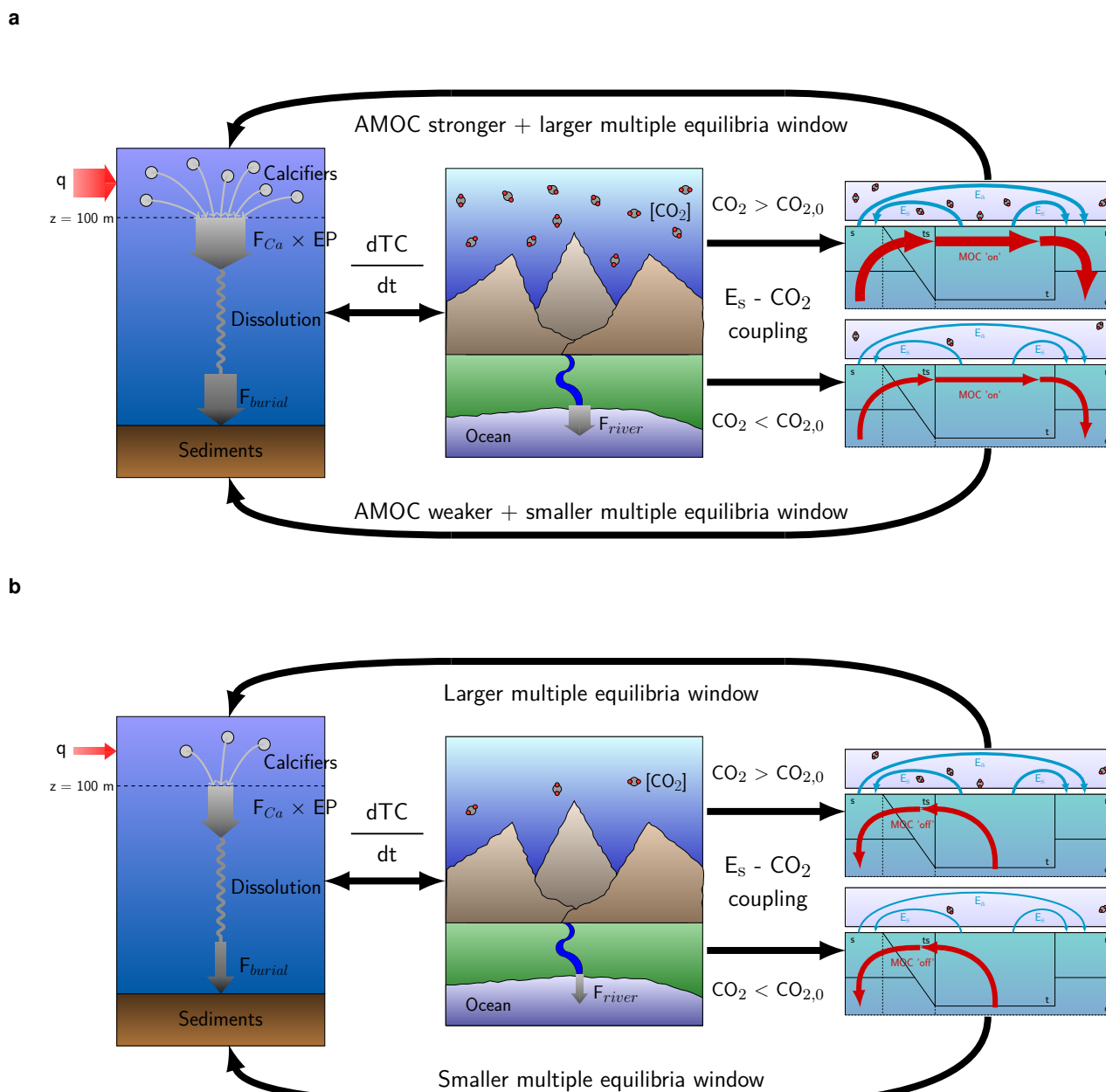


Figure 6. Illustrations of the main mechanisms affecting atmospheric pCO_2 and AMOC stability. Panel a shows the mechanisms for the on-branch. A strong AMOC increases export production through increased nutrient advection (left panel), which is accompanied by a high atmospheric pCO_2 due to the necessary balance between the river influx and sediment burial (middle panel). If the CO_2 concentration is larger (smaller) than $CO_{2,0}$ than the AMOC will strengthen (weaken) and the MEW increases (decreases) (right panels). Panel b shows the mechanisms for the off-branch. The absence of an AMOC decreases export production through decreased nutrient advection (left panel), accompanied by a low atmospheric pCO_2 (middle panel). When pCO_2 is larger (smaller) than $pCO_{2,0}$ the MEW increases (decreases) (right panel).

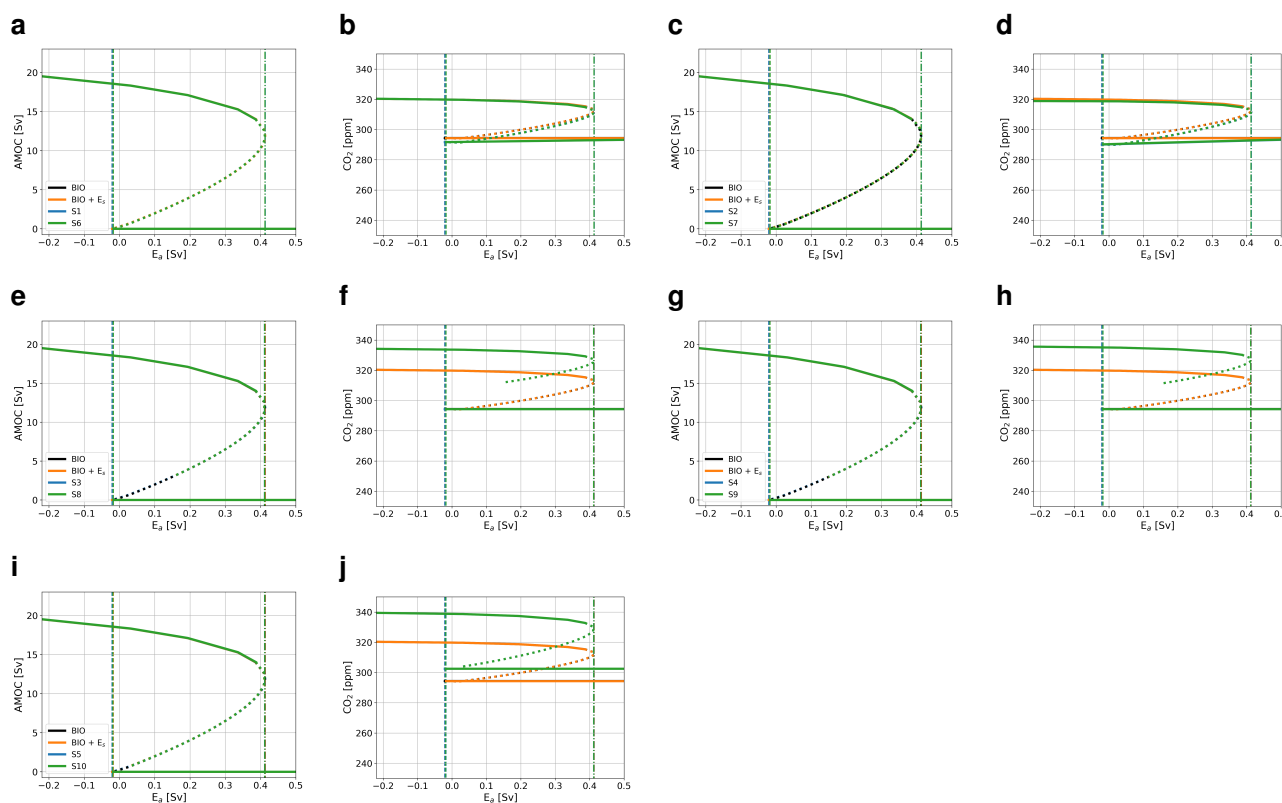


Figure A1. Bifurcation diagrams showing the sensitivity of the model to E_a for additional cases as defined in Table A1. Solid lines represent stable steady state solutions, dotted lines represent unstable states, dash-dotted lines represent the location of the saddle node on the on-branch, and dashed lines the location of the saddle node on the off-branch. The black lines represent a case with only the biological coupling (BIO), the orange lines with the logarithmic CMIP6 based E_s and biological coupling ($E_s + \text{BIO}$), and the blue and green lines represent the cases defined in Table A1. Results are for the AMOC strength in Sv (a, c, e, g, i) and atmospheric $p\text{CO}_2$ in ppm (b, d, f, h, j).